Glacial ice sheet extent effects on modeled tidal mixing and the global overturning circulation

Wilmes, Sophie-Berenice; Schmittner, Andreas; Green, Mattias

Paleoceanography

Glacial ice sheet extent effects on modeled tidal mixing and the global overturning circulation

S. B. Wilmes,[1,2] A. Schmittner,[1] J. A. Mattias Green,[2]

_____

[1]College of Environmental, Atmospheric

and Ocean Sciences, Oregon State

University, Corvallis, Oregon, USA.

[2]School of Ocean Sciences, Bangor

University, Menai Bridge, Ynys Môn, UK.

Key Points.

○ Modeled deep ocean tidal dissipation approximately doubled during the LGM but the magnitude is affected by uncertainties in LGM ice sheet extent.

○ Increase in LGM tidal mixing enhances diffusivities in the LGM ocean, especially in the Atlantic.

○ Including LGM tidal mixing in climate model simulations strengthens the LGM MOC, and alters ocean temperature and salinity distributions.

At present, tides supply approximately half (1 TW) of the energy necessary to sustain the global deep meridional overturning circulation (MOC) through diapycnal mixing. During the Last Glacial Maximum (19,000–26,500 years BP; LGM) tidal dissipation in the open ocean may have strongly increased due to the 120–130 m global mean sea-level drop and changes in ocean basin shape. However, few investigations into LGM climate and ocean circulation consider LGM tidal mixing changes. Here, using an intermediate complexity climate model we present a detailed investigation on how changes in tidal dissipation would affect the global MOC. Present-day (PD) and LGM tidal constituents M_2, S_2, K_1 and O_1 are simulated using a tide model, and accounting for LGM bathymetric. The tide model results suggest that the LGM energy supply to the internal wave field was 1.8–3 times larger than present and highly sensitive to Antarctic and Laurentide ice sheet extent. Including realistic LGM tide forcing in the LGM climate simulations leads to large increases in Atlantic diapycnal diffusivities, and strengthens (by 14–64% at 32°S) and deepens the Atlantic MOC. Increased input of tidal en-

ergy leads to a greater draw-down of North Atlantic Deep Water and mix-

ing with Antarctic Bottom Water altering Atlantic temperature and salin-

ity distributions. Our results imply that changes in tidal dissipation need be

accounted for in paleo-climate simulation setup as they can lead to large dif-

ferences in ocean mixing, the global MOC, and presumably also ocean car-

bon and other biogeochemical cycles.

1. Introduction

The meridional overturning circulation (MOC) is an important component of the Earth's climate system redistributing large amounts of heat, freshwater and momentum across the globe [*Wunsch and Ferrari*, 2004] with the Atlantic MOC (AMOC) being a key part of the system. In the modern ocean the AMOC is characterized by two overturning cells: one upper cell in which warm and salty water flows northward from the tropics losing heat to the atmosphere and supplying the formation of North Atlantic Deep Water (NADW) in the Nordic and Labrador Seas which flows southwards, occupying the deep North Atlantic; and one 'deep' cell in which Antarctic Bottom Water (AABW) flows northward in the deepest parts of the Atlantic, gradually mixing with the lower portions of NADW (see e.g. *Talley et al.* [2011]). The global MOC is maintained by diapycnal mixing in the thermocline and deep ocean driven by the tides and the wind with each supplying around 1 TW of energy [*Wunsch and Ferrari*, 2004].

The strength and structure of the AMOC during the Last Glacial Maximum (26.5 – 19 kyr BP; henceforth LGM; see e.g. *Peltier and Fairbanks* [2006] or *Clark et al.* [2009]), however, remains contended. Studies reconstructing the AMOC from nutrient tracers [*Sigman et al.*, 2010; *Skinner et al.*, 2010; *Muglia et al.*, 2018] infer a more sluggish and shoaled water mass in the North Atlantic, together with a stronger influx of southern sourced waters in the deep North Atlantic; whereas others suggest a shoaling of North Atlantic Deep Water (NADW) but with vigorous overturning [*Curry and Oppo*, 2005; *Howe et al.*, 2016; *Keigwin*, 2004; *Marchitto and Broecker*, 2006; *Bradtmiller et al.*, 2014; *Gherardi et al.*, 2009; *Lippold et al.*, 2012; *Lynch-Stieglitz*, 2017; *Kurahashi-Nakamura*

et al., 2017]. Theoretical concepts that link AMOC shoaling to sea ice expansion in the

Southern Ocean have been proposed suggesting reduced mixing of NADW with Antarctic

Bottom Water.

Further studies put forth that the water mass structure may have been similar to today's

AMOC [Gebbie, 2014]. The latest Paleo-Model Intercomparison Project (PMIP3) models

generally show a strengthened AMOC and a deepened NADW cell for the LGM [Muglia

and Schmittner, 2015], whereas the older generation of models (PMIP2) showed more

conflicting results with some showing a strengthened AMOC and others indicating a

weakened overturning [Otto-Bliesner et al., 2007; Weber et al., 2007].

A number of studies have proposed that the 120–130 m sea-level drop (SLD) during

the LGM exposing most continental shelves lead to a shift of tidal dissipation from the

highly energetic present-day shelf seas into the deep ocean, where tidal dissipation in the

semi-diurnal band increased by around a factor of two [Arbic et al., 2004; Egbert et al.,

2004; Griffiths and Peltier, 2009; Green, 2010; Wilmes and Green, 2014]. It has been

suggested that parts of the ocean such as the North Atlantic are close to resonance at

M_2 frequencies (see e.g. Platzman et al. [1981] or Müller [2008]) and the removal of the

shelf seas during the LGM reduces the damping of the ocean and thus increases tides and

dissipation in the deep ocean [Egbert et al., 2004; Green, 2010], especially throughout the

Atlantic [Egbert et al., 2004; Green et al., 2009; Green, 2010; Wilmes and Green, 2014],

where it could affect the MOC. Previous work [Griffiths and Peltier, 2009; Wilmes and

Green, 2014] also suggests that the extent to which dissipation increases may be sensitive

to the location of the grounding-line around Antarctica. The most recent reconstructions

of LGM ice sheet extent around Antarctica by *Hillenbrand et al.* [2014] show that the

grounding line in the Weddell Sea during the LGM cannot be unambiguously constrained

and may have either been located at the shelf break with grounded ice occupying the

entire shelf or else it could have been situated much further southward in some areas

giving rise to the possibility of large ice shelves in the Weddell Sea area.

Enhancements in tidal dissipation during the LGM have been expected to increase the

amount of energy available to the internal tide and hence for diapycnal mixing [*Wunsch*,

2003; *Egbert et al.*, 2004; *Green et al.*, 2009; *Schmittner et al.*, 2015], however, climate

model (see e.g. *Otto-Bliesner et al.* [2007], *Kageyama et al.* [2017]) or conceptual [*Ferrari

al.*, 2014] studies of LGM ocean circulation generally assume present-day tidal mix-

ing despite considering a variety of other boundary condition changes or apply spatially

uniform tidal mixing changes [*Kurahashi-Nakamura et al.*, 2017].

Previous modeling work [*Schmittner et al.*, 2015; *Green et al.*, 2009; *Montenegro et al.*,

2007] has investigated the impact of altered tidal mixing on the LGM AMOC, however,

with conflicting results. *Montenegro et al.* [2007] indicate negligible effects of LGM tides

on the AMOC, whereas *Schmittner et al.* [2015] report a substantial strengthening and

deepening of the overturning cell in the North Atlantic. There have been some attempts

model tides and ocean circulation in an ocean model setup that explicitly models tidal

dynamics at the same resolution as the ocean general circulation (see e.g., *Müller et al.*

[2010], *Müller et al.* [2012], *Weber et al.* [2017]). However, the tide models in these config-

urations either are less accurate due to their low resolution, or else at higher resolution the

computational expense of the ocean model becomes prohibitive for multimillenial-length

91 simulations necessary for the LGM. Here, we take the approach of separately modelling

92 the tides and ocean circulation, in order to capture small scale variations in the tide ac-

93 curately with a high resolution tide model, and use an intermediate complexity ocean

general circulation model suitable for long-term simulations.

The overarching aim of this work is to investigate in more detail possible impacts of

96 changes in tidal dissipation on the LGM MOC and to expand on the work by *Schmittner*

97 *et al.* [2015] by providing a more comprehensive uncertainty analysis. Specific aims are to

98   1. compare the impact of different internal wave drag parameterizations on LGM tidal

dissipation estimates,

2. determine the impact of different LGM ice extent and sea-level change estimates on

101 LGM tidal dissipation, and

102   3. analyze effects and uncertainties of LGM tidal dissipation changes on the MOC,

103   4. contrast the individal and combined effects of LGM tidal dissipation changes and

104 wind effects on the MOC, thereby building on *Schmittner et al.* [2015] and *Muglia and*

Schmittner [2015].

We present a series of sensitivity experiments designed to test which processes the

simulated tidal energy dissipation and MOC are most sensitive to. We do not attempt

108 to simulate a realistic LGM MOC, which requires comparison to paleo data and will be

109 published elsewhere. The paper is structured as follows: In the methodology we introduce

the tidal model and the climate model and detail the experiments; in the results section

111 we will first present the tide modeling results and then discuss the results from the climate

model simulations. The study will be concluded with a discussion tying our results in with

previous work.

2. Methodology

2.1. Tide model

The Oregon State Tidal Inversion Software (OTIS) has been widely used for modeling tides in both regional and global applications for the past, present and future [*Egbert et al.*, 2004; *Green*, 2010; *Pelling and Green*, 2013; *Wilmes and Green*, 2014; *Green et al.*, 2017; *Wilmes et al.*, 2017]. OTIS solves the linearized shallow water equations [*Egbert et al.*, 2004] which are given by

$$\frac{\partial \mathbf{U}}{\partial t} + \mathbf{f} \times \mathbf{U} = -gH\nabla(\zeta - \zeta_{EQ} - \zeta_{SAL}) - \frac{c_d|U|U}{H^2} - \frac{\mathbb{C}_{IT} \cdot U}{H} \tag{1}$$

$$\frac{\partial \zeta}{\partial t} = -\nabla \cdot \mathbf{U}, \tag{2}$$

where $\mathbf{U} = \mathbf{u}H$ is the depth integrated volume transport, which is calculated as tidal current velocity $\mathbf{u}$ times water depth H. f is the Coriolis vector, g denotes the gravitational constant, ζ stands for tidal elevation, ζ_{SAL} denotes the tidal elevation due to self-attraction and loading, and ζ_{EQ} is the equilibrium tidal elevation. $\frac{c_d|U|U}{H^2}$ and $\frac{\mathbb{C}_{IT} \cdot U}{H}$ represent drag due to bed friction and internal tides (IT), respectively (see Section 2.1.2 for details). The spatially uniform drag coefficient, c_D, is set to 0.003. These equations are solved on an Arakawa C-grid, using explicit finite differences time stepping, with periodic forcing, followed by harmonic analysis of the steady state solution to obtain tidal elevations and transports [*Egbert et al.*, 2004, 1994]. OTIS is run for M_2, S_2, K_1 and O_1 at 1/8° horizontal resolution for 23 days with the last 17 days being used for harmonic analysis. The

129 model is run in a near-global set up with a full longitudinal extent and ranging from 86°

130 S to 89° N. At the northern open boundary we prescribe elevation boundary conditions

131 from the TPXO7.2 database. For a discussion on applying open boundary conditions for

132 paleo-tide simulations see *Wilmes and Green* [2014].

2.1.1. Bathymetry and LGM sea-level changes

134 The present-day bathymetry comes from the RTOPO2 database [see *Schaffer et al.*,

135 2016, and `https://doi.pangaea.de/10.1594/PANGAEA.856844` for the latest version]

136 which has been averaged to 1/8° degree horizontal resolution. For the LGM bathyme-

137 tries we use sea-levels from the ICE-5G (VM2 L90) version 1.2 [*Peltier*, 2004] and ICE-

138 6G (VM5a) [*Argus et al.*, 2014; *Peltier et al.*, 2015] databases (both obtained from

139 `http://www.atmosp.physics.utoronto.ca/~peltier/data.php`) for the present day

140 and 21 kyr BP. The sea-level difference between the present-day and the LGM was calcu-

141 lated by subtracting the present-day sea-levels from the LGM sea-levels in the respective

142 ICE-5G or ICE-6G dataset. The lower-resolution paleo sea-level changes (1° degree hori-

143 zontal resolution) are then interpolated to the 1/8° degree grid and added to present-day

144 RTOPO2 bathymetry in order to retain higher-resolution topographic features. Land ice

145 present in ICE-5G or ICE-6G is assumed to be fully grounded and is set to land in the

146 high-resolution LGM bathymetries. Both the sea-level changes between the present-day

147 and the LGM, and the LGM ice extent slightly differ between ICE-5G and ICE-6G, with

148 discrepancies being especially prominent in the Weddell Sea and the Ross Sea. These

149 differences and their implications for LGM tides will be investigated in the results section

150 with sensitivity experiments detailed in Section 2.3.1. Additional experiments reproduc-

151 ing the setup by *Montenegro et al.* [2007] are detailed in the Supplementary Materials

152 (Suppl. Text S1).

153 **2 1.2. Tidal energy conversion**

The loss of energy to the internal tide is parameterized through a spatially varying

dr g tensor $\mathbb{C}_{IT}$. Various schemes have been proposed to calculate $\mathbb{C}_{IT}$ which tend to

156 be a function of topographical roughness, buoyancy frequency, Coriolis parameter, wave

157 number and tidal frequency [e.g. *Bell*, 1975; *Jayne and St.Laurent*, 2001; *Nycander*, 2005;

158 *Zaron and Egbert*, 2006] and a selection of schemes were contrasted in *Green and Nycander*

[2 13]. Here, we shall apply the tidal conversion parameterizations by *Zaron and Egbert*

160 [06] (ZE) and *Jayne and St.Laurent* [2001] (JS). For the ZE scheme, $\mathbb{C}_{IT}$ is given by

161 the tensor

$$\mathbb{C}_{ZE} = \Gamma H (\nabla H)^2 \frac{N_b \bar{N}}{8\pi^2 \omega}, \tag{3}$$

162 where Γ is a tuning factor originally set to 50 and H is water depth. N_b and and $\bar{N}$ are

163 buoyancy frequency at the sea-bed ($z = -H$) and mean buoyancy frequency, respectively.

is the tidal frequency of the respective tidal constituent. The ZE scheme originally uses

 ameterized bottom and mean buoyancy frequencies; however, in order to account for

po sible variations in stratification in the glacial ocean, we here use N_b and $\bar{N}$ calculated

167 from temperatures and salinities from the WOA 2013 v2 database (*Locarnini et al.* [2013]

168 ar l *Zweng et al.* [2013]; see `https://www.nodc.noaa.gov/OC5/woa13/woa13data.html`

for the latest version).

170 The JS scheme includes no directional variations in $\mathbb{C}_{IT}$ and the ITdrag therefore becomes

171 a spatially varying scalar calculated as follows:

$$C_{JS} = \frac{\pi}{L}\hat{H}^2 N_b, \tag{4}$$

172 where L is a topographical length scale set to 10,000 m in the original work, $\hat{H}^2$ is the

173 standard deviation of the topography and N_b is observed bottom buoyancy frequency. $\hat{H}^2$

174 represents subgrid-scale topographic variations and is calculated from the 1' original data

175 base.

176 The conversion of energy from the barotropic to baroclinic tide depends on stratification

177 (see Equations 3 and 4). Our tide model experiments use present-day stratification fields.

178 However, we have performed simulations where temperature and salinity anomalies from

179 a range of LGM circulation configurations from *Muglia et al.* [2018] were added to the

180 present-day temperature and salinity stratification fields and stratification was recalcu-

181 lated. Some of the input fields had high abyssal salinities and increased deep stratification

182 consistent with *Adkins et al.* [2002]'s reconstructions. We find very weak sensitivity to

183 the resulting changes in bottom and mean buoyancy frequency. Globally integrated dis-

184 sipation for the runs using LGM stratification fields lies within ±0.1 TW of the globally

185 integrated dissipation of the tidal simulations used to force the climate model [see also

186 *Egbert et al.*, 2004; *Green and Huber*, 2013, for further discussions on the topic]. This

187 is also consistent with the results from *Schmittner et al.* [2015] who applied an iterative

188 procedure for updating the stratification field in the tide model with output from the

189 climate model and then re-runnning the tide model and subsequently the climate model.

191 **2.1.3. Tuning and model evaluation**

Both ITdrag schemes contain a tunable parameter (Γ and L, respectively). Here, we modify the tuning factors in order to obtain tidal amplitudes and open ocean dissipation values as realistic as possible. The tuning factors used for our simulations are shown in Table 1. It is worth noting that for different model resolutions different tuning factors are required as the roughness of the topography (given by $(\nabla H)^2$ and $\hat{H}^2$, respectively) changes with resolution. The simulations are evaluated against the TPXO8 global barotropic tidal atlas [see *Egbert and Erofeeva*, 2002, and http://volkov.oce.orst.edu/tides/tpxo8_atlas.html for the latest version]. We calculate latitudinally weighted amplitude root-mean square errors together with dissipation for both the global ocean and the deep ocean.

2.2. Calculation of dissipation

Two different methods can be applied to calculate tidal dissipation. Firstly, the tidal dissipation due to both bed friction D_B and internal tide conversion D_{IT} can be calculated directly, provided the mechanism by which the energy is lost, i.e. $\mathbb{C}_{IT}$, is known. It is worth noting that the tidal conversion parameterization shows up at the locations where energy is lost from the barotropic tide to the baroclinic tide but not where the internal waves finally dissipate their energy. The corresponding equations of the 'direct method' are

$$D_B = \rho_0 c_d |u| u^2 \text{ and} \tag{5}$$

$$D_{IT} = \rho_0 \mathbb{C}_{IT} u^2 \tag{6}$$

where ρ_0 is reference density, which is set to 1035 kg/m^3.

In contrast, the method put forth by *Egbert and Ray* [2001] calculates the work balance of the tides (henceforth referred to as the 'energy balance method') without knowledge of the mechanism by which the energy is lost. Here the dissipation D is calculated as the balance between the work done by the tide, W, and the divergence of the energy flux, P:

$$D = W - \nabla \cdot P \tag{7}$$

where W and P are given by

$$W = g\rho_0 \langle U \cdot \nabla(\zeta_{EQ} + \zeta_{SAL}) \rangle, \text{ and} \tag{8}$$

$$P = g\rho_0 \langle U\zeta \rangle, \tag{9}$$

where $\langle \rangle$ denote time averages. This method has advantages for the calculation of dissipation from e.g. assimilated tidal solutions such as TPXO as, apart from tidal elevations and transports, only the astronomic tide forcing needs to be known and will therefore be used for the evaluation of the present-day simulation in comparison to TPXO8. Elsewhere in the manuscript dissipation will be calculated with the direct method unless otherwise specified.

2.3. Tide model simulations

We carry out present-day simulations at 1/8° horizontal resolution for both ZE and JS ITdrag. For the LGM (here, 21 kyr BP) we carry out simulations for realistic sea-level changes from both ICE-5G and ICE-6G for each ITdrag. Additionally, for comparison with the next set of runs, we also perform simulations with sea-level uniformly lowered

by 120 m. For the simulations reproducing the *Montenegro et al.* [2007] results see Supplementary Text S1.

2.3.1. Sensitivity simulations

Additionally, we carry out simulations for M_2 only to test for the sensitivity to the differences in mean sea-level change and ice extent between ICE-5G and ICE-6G. To test for sea-level sensitivity we perform simulations with a uniform SLD of 100 m, 110 m, 120 m, 130 m and 140 m with each ICE-5G and ICE-6G landmasks, respectively. For sensitivity to ice-sheet extent we start from the LGM ICE-5G case and incrementally block the Weddell Sea until the ice extent is that found in ICE-6G (denoted 'ICE-5G blk1' to 'ICE-5G blk5'). In the next step the ICE-6G landmask is applied in the northern hemisphere (denoted 'ICE-5G blk5 + NH ice6g lnd').

2.4. Climate model

The climate model simulations are carried out with the University of Victoria Earth System Climate Model (UVic) [*Weaver et al.*, 2001] version 2.9 [*Eby et al.*, 2009] in the same setup at *Schmittner et al.* [2015]. UVic has a three-dimensional ocean-general-circulation model coupled to a one-layer energy-moisture balance atmosphere and a thermodynamic sea-ice model. It has a horizontal resolution of $3.6 \times 1.8°$ with 19 vertical layers. The model is forced with seasonally varying top-of-the-atmosphere solar irradiance, wind stress, cloud albedo and moisture advection velocities. The model setup for this study uses the tidal mixing parameterization by *Schmittner and Egbert* [2014], based on *Jayne and St.Laurent* [2001] and *Simmons et al.* [2004], which includes effects of subgrid-scale bathymetry on the depth of energy input and distinguishes between diurnal and semi-diurnal tides. The

diapycnal diffusivity, k_v, is given by

$$k_v = k_{bg} + \frac{\Gamma \epsilon}{N^2}, \tag{10}$$

where k_{bg} is the background diffusivity which is set to 0.3×10^{-4} m^{2}s^{-1} and includes the effect of remotely dissipated tidal energy and mixing through other processes. Γ is the mixing efficiency which is set to 0.2 and N^2 is the buoyancy frequency. The rate of tidal energy dissipation, ϵ is

$$\epsilon = \frac{1}{\rho} \sum_{z'>z}^{H} \sum^{TC} q_{TC} D_{IT,TC}(x,y,z') F(z,z'), \tag{11}$$

where $D_{IT,TC}(x,y,z')$ is the energy flux from the barotropic to the internal tide from the high-resolution tide model, D_{IT}, mapped onto the climate model grid accounting for subgrid-scale bathymetric effects in the horizontal (thus the dependence on z'; for a more detailed description see *Schmittner and Egbert* [2014]). F is the vertical decay-function using an e-folding depth of 500 m above the sea floor H. q_{TC}, the local dissipation efficiency, accounts for the critical latitude y_c of diurnal and semi-diurnal tidal constituents (TC):

$$q_{TC} = \begin{cases} 1, \text{for } |y| > y_{c,TC} \\ 0.33, \text{ otherwise.} \end{cases} \tag{12}$$

y_c is 30° for the diurnal constituents K$_1$ and O$_1$, and 72° for the semi-diurnal constituents M$_2$ and S$_2$.

Paleo-boundary conditions for the LGM simulations include prescribed ice sheets [*Peltier*, 2004], orbital parameters altering latitudinal and seasonal distributions of solar irradiance and atmospheric CO$_2$ concentrations. In the LGM simulations CO$_2$ levels are lowered to 185 ppm in contrast to 280 ppm in the preindustrial control simulations.

Changes in other greenhouse-gas concentrations are neglected here. The bottom topography is kept constant between the pre-industrial and LGM setup. Wind forcing is either kept at preindustrial control levels (denoted "PD winds") or LGM anomalies from the PMIP3 ensemble average were added as in *Muglia and Schmittner* [2015] (denoted "LGM winds"). PMIP3 experiments were based on a blended ice sheet reconstruction (ICE-6G, ANU and MOCA) whereas our LGM UVic simulations using LGM tidal fields based on either ICE-5G or ICE-6G. This slight inconsistency will likely have only minor effects on the results since the main effect of wind changes, an increase over the North Atlantic caused by the presence of the Laurentide ice sheet [*Muglia and Schmittner*, 2015], is likely to be a robust first order effect regardless of the specific ice reconstruction, consistent with only minor effects of different ice reconstructions on the MOC found by *Vettoretti and Peltier* [2013].

2.5. Climate model simulations

The following climate model simulations are carried out. The preindustrial control simulation (denoted 'PIC') has pre-industrial climate forcing, PD winds and PD ZE 1/8° TOPO2 tide fields. Six LGM simulations are performed:

1. PD tides and PD winds ('LGM_pdT_pdW')

2. PD tides and LGM winds ('LGM_pdT_lgmW')

3. LGM ICE-5G tides and PD winds ('LGM_i5gT_pdW')

4. LGM ICE-5G tides and LGM winds ('LGM_i5gT_lgmW')

5. LGM ICE-6G tides and PD winds ('LGM_i6gT_pdW')

6. LGM ICE-6G tides and LGM winds ('LGM_i6gT_lgmW')

285 For the simulations reproducing the *Montenegro et al.* [2007] results see Supplementary

286 Text S1.

3. Results

3.1. Tide modeling

3.1.1. Present-day run evaluation

287 All present-day simulations are summarized and compared to TPXO8 in Table 1. The

two higher resolution simulations at 1/8° horizontal resolution show considerably lower

290 root-mean square M_2 amplitude errors (RMSE) in comparison to TPXO8. In the deep

291 ocean ($h > 500$ m) the M_2 RMSE for PD_ZE_1_8 has an RMSE of below 4 cm whereas

for PD_JS_1_8 it is slightly higher at 4.5 cm. All runs show realistic total and deep

293 dissipation values in comparison with TPXO8 (using the energy balance method yields

294 a total dissipation of 3.1 TW and 1.2 TW in the deep ocean for TPXO8). The energy

295 balance method and the direct method for the dissipation calculation yield similar (within

20%) deep and total dissipation values and from here onwards only the direct method shall

297 be used.

3.1.2. LGM tides

299 The model produces large increases in deep dissipation for the LGM simulations (see

300 Figs. 1 and 2), mainly due to the M_2 tidal constituent. For the ICE-5G case, deep

dissipation approximately triples to 3.4 TW for ZE ITdrag and to 2.9 TW for JS, in

302 line with previous estimates of deep dissipation during the LGM [*Egbert et al.*, 2004;

303 *Griffiths and Peltier*, 2009; *Green*, 2010; *Wilmes and Green*, 2014; *Schmittner et al.*,

2015]. In contrast to the ($\sim$)2 TW increases for ICE-5G the dissipation increase for ICE-

6G is halved to only ∼1 TW for both ZE and JS. This is a somewhat surprising result given that ICE-6G is an updated version of ICE-5G. For both the ICE-5G and ICE-6G simulations large increases in dissipation take place throughout the Atlantic and are especially pronounced at mid latitudes both in the North and South Atlantic. For ICE-5G the increases also extend into the western Indian Ocean. The runs with ZE ITdrag result in dissipation increases in the Atlantic by almost a factor of 8 for ICE-5G and by about a factor of 3 for ICE-6G. In comparison to ICE-5G the ICE-6G dissipation changes are considerably reduced both in the North and South Atlantic and also around the equator where dissipation decreases are seen. Throughout the Pacific (increases of 56 and 53% for ICE-5G and ICE-6G, respectively) and eastern Indian Ocean the dissipation changes are very similar regardless of the LGM bathymetry used. The integrated Indian Ocean dissipation more than doubles in ICE-5G (ZE ITdrag) but shows no change in ICE-6G. Both the ZE ITdrag and JS ITdrag simulations show very similar responses in dissipation for the two LGM scenarios; as the ZE simulations agree better with present day tide observations this ITdrag parameterization will be used for the high resolution simulations from this point onwards.

3.1.3. Reasons for the large differences between ICE-5G and ICE-6G

al mean sea-level in the LGM ICE-5G bathymetry is on average 122 m lower than at present whereas for ICE-6G the sea-level drop is reduced to 114 m at 21 kyr BP. Large differences can be seen in the land mask between ICE-5G and ICE-6G, which are especially prominent in the Weddell Sea due to differences in ice extent in the two versions (Fig. 3a). In order to test the sensitivity of the tides to the mean sea-level decrease we

perform simulations where sea-level is uniformly decreased by 110–140 m and the land

mask for either ICE-5G or ICE-6G is applied (see Fig. 1).

These simulations highlight that the tides are remarkably insensitive to the mean sea-level change as an additional sea-level decrease by 30 m increases dissipation by only 0.2 TW. These simulations indicate that differences in mean sea level cannot be causing most of the large differences in dissipation between ICE-5G and ICE-6G. Incrementally advancing the ice (land mask) in the Weddell Sea from the ICE-5G to the ICE-6G position (blk 1 – blk 5; see Fig. 3b) decreases M_2 deep dissipation by 0.9 TW (Fig. 3 c). This dissipation increase occurs mainly in the South Atlantic suggesting that dissipation enhancement in the South Atlantic for LGM ICE-5G is very sensitive to the LGM ice position in the Weddell Sea (Suppl. Fig. S2 a and b). Additionally, applying the ICE-6G land mask in the Northern Hemisphere leads to a further decrease in dissipation by 0.4 TW to levels very close to the dissipation values in ICE-6G. Modifying the Northern Hemisphere land mask leads to decreases in dissipation in the North Atlantic (Suppl. Fig. S2 c and d) and a dissipation change pattern very closely resembling the LGM ICE-5G case. These results suggests that the LGM tides were very sensitive to even small changes in ice extent (land-sea boundaries) both in the North and South Atlantic. These findings are consistent with results by *Wilmes and Green* [2014] who suggest that global tidal dissipation during the LGM may be sensitive to ice extent in the Weddell Sea.

3.2. Climate modeling

3.2.1. Preindustrial control

In the PIC, the AMOC at 25°N has a strength of 16.0 Sv at 25° N which is in good correspondence and within the error margins of present-day estimates of 17.5 Sv [*McCarthy et al.*, 2012; *Schmittner and Egbert*, 2014] (see Table 2 and Fig. 4). The model estimates of Atlantic Antarctic Bottom Water (Atl AABW) strength and Circumpolar Deep Water export to the Indian Ocean (CPDW Indian) and Pacific Ocean (CPDW Pacific) are 1–2 Sv lower than the present-day estimates but within the error margins of the observational means. The overall root-mean square error for the differences between the PIC and the observations is 2.0 Sv which is approximately halved with respect to the values presented Schmittner and Egbert [2014] who used older tidal dissipation fields from *Jayne and Laurent* [2001] and *Egbert and Ray* [2003] with higher globally integrated internal tide flux together with a background diffusivity of 0.15 x 10^{-4} m^2s^{-1} rather than the 0.3 x 10^{-4} m^2s^{-1} in this study.

Diffusivities in the PIC are in good agreement with observations (the values reported in brackets are the average and range from Table 2 in *Waterhouse et al.* [2014]'s compilation; all in 10^{-4} m^2s^{-1}) with globally averaged k_v from 250 m to 5000 m being 1.4 10^{-4} m^2s^{-1} (3.3, 0.2-8.6), from 250 m to 1000 m 0.5 10^{-4} m^2s^{-1} (0.3, 0.2-0.4) and from 1000 m to 5000 m 1.7 10^{-4} m^2s^{-1} (4.3, 0.4-11.5). The model values lie within the error range of the observations except for the shallow waters for which they still lie within a factor 2 of the observational mean. It is also worth noting that data in *Waterhouse et al.* [2014] is somewhat patchy, especially in the central parts of the Pacific and Atlantic, possibly biasing the means.

3.2.2. LGM simulations

369   Large increases in tidal dissipation in comparison to the present-day case also result

370   when dissipation is mapped onto the climate model grid (Suppl. Fig. S3). The increases

371   in horizontally integrated dissipation in ICE-5G are especially pronounced between ∼500

      and 3500 m and range between 160 and 260% in these depth layers. For ICE-6G the

      increases are smaller with dissipation increases more uniformly with depth between 60

374   and 100%.

375   In LGM_pdT_pdW the horizontally averaged Atlantic k_v profile closely reflects the PIC

376   case apart from relatively small mid-depth increases in the Southern Ocean sector (Fig. 5).

      These minor changes are due to changes in stratification (see Eq. 10). In contrast, for

378   both LGM_i5gT_pdW and LGM_i6gT_pdW strong mid-depth enhancements in Atlantic

379   diffusivities occur which are greatest for the ICE-5G tide forcing (with increases of up to

380   280%) and approximately halved for ICE-6G. This illustrates that stratification changes in

      the climate model have a much smaller impact on vertical diffusivities and the MOC than

382   changes in tidal energy dissipation. The increases in k_v mainly take place at mid latitudes

383   in the North and South Atlantic where increases of nearly an order of magnitude can be

384   seen for LGM_i5gT_pdW (Fig. 4). For LGM_i6gT_pdW similar but less pronounced (up

      to 400%) increases can be seen. These diffusivity increases reflect closely the increases in

      tidal energy dissipation discussed above (Fig. 2).

387   The large increases in diffusivities due to the LGM tidal dissipation forcing lead to a

388   strengthening of the overturning in the Atlantic (see Table 2 and Fig. 4). The AMOC at

      N increases from 10.2 Sv in lgm_pdT_pdW to 14.0 Sv in lgm_i5gT_pdW and to 13.0 Sv

390   in lgm_i6gT_pdW. AABW flow into the Atlantic in lgm_i5gT_pdW is reduced by 14% due

to a substantial deepening of the AMOC. In contrast, AABW changes by less than 3% in lgm_i6gT_pdW despite of an increase in the AMOC by nearly 30%, presumably because the AMOC is not deepening as much as in the ICE-5G case. ICE-5G tide forcing increases the export of CPDW into the Indian Ocean sector by 1.7 Sv (see Suppl. Fig. S4) due to strengthened tidal dissipation in the eastern Indian Ocean whereas for the simulations forced with LGM ICE-6G tides, where dissipation changes in the Indian Ocean are small, no change in CPDW inflow occurs in comparison to lgm_pdT_pdW. In contrast, whilst CPDW export into the Pacific increases with LGM tidal forcing, the increases are slightly weaker for ICE-6G forcing than for ICE-5G. Integrated basin-wide dissipation values for the Pacific are very similar though, which suggests that the weaker CPDW export into the Pacific in ICE-6G is due to the weaker AMOC and export of NADW into the Southern Ocean.

The increased LGM tidal mixing deepens the mixed layer in the North Atlantic in lgm_i5gT_pdW by over 1000 m with the largest increases taking place between 50°N and 60°N in the central North Atlantic, at the south-west of the southern tip of Greenland and to the south of Iceland (see Suppl. Fig. S5). In lgm_i6gT_pdW similar but less pronounced increases in mixed layer depth can be seen around the southern tip of Greenland and south of Iceland. The increase in LGM tidal dissipation leads to enhanced mixing of southern sourced and northern sourced Atlantic water masses. This increases bottom water (below 3000 m) temperatures and salinities in the Atlantic (see Fig. 6) due to the higher proportion of NADW in lgm_i5gT_pdW and lgm_i6gT_pdW in contrast to lgm_pdT_pdW where Atl AABW dominates the deep North Atlantic. In the equatorial

413 and north Atlantic temperatures and salinities decrease at mid depths in comparison to

414 lgm_pdT_pdW due to the higher proportion of fresher and colder Atl AABW being mixed

415 upwards in lgm_i5gT_pdW and lgm_i6gT_pdW.

The strengths of the subpolar and subtropical gyres in the North Atlantic are in-

creased with respect to lgm_pdT_pdW (see Suppl. Fig. S5). For ICE-5G tide forcing

418 the strength of the subpolar gyre increases from 9 Sv in lgm_pdT_pdW to 16 Sv and 12

419 Sv in lgm_i5gT_pdW and lgm_i6gT_pdW, respectively. The changes in subtropical gyre

420 strength are less pronounced, but follow the same pattern.

The stronger AMOC and strengthened gyre circulation in lgm_i5gT_pdW and

422 lgm_i6gT_pdW result in an increase in northward Atlantic heat transport between 40°S

423 and 60°N which is approximately twice as large for ICE-5g tidal mixing than for ICE-6G

424 (see Fig. 7). Meridional northward salt fluxes increase between 50° N and 65°N and are

related to the increase in strength of the subpolar gyre.

426 Adding PMIP3 ensemble mean LGM wind anomalies to the present-day wind forcing

427 applied in lgm_pdT_pdW increases the AMOC strength by 2.9 Sv in lgm_pdT_pdW to 13.1

428 Sv and adds a secondary maximum in the streamfunction between 50°N and 60°N (Fig. 4).

The AMOC increase is linked to an increase in the northward salt fluxes in the North

Atlantic (see *Muglia and Schmittner* [2015] and Fig. 7) due to increases in the strength

431 of both the subpolar (increase by a factor of 3) and the subtropical gyre (strengthened

432 by factor of 1.6) together with an increase in the southward extent of the subpolar gyre

(see Suppl. Fig. S5). This leads to an increase in sea surface salinities in the North

434 Eastern Atlantic north of 45°N and a decrease in surface salinities in the subtropical

Atlantic. Mid-depth temperatures in the North Atlantic strongly decrease but bottom water temperatures show no change in comparison to lgm_pdT_pdW (Fig. 6). AABW salinities show small enhancements (Fig. 6). Changes in wind forcing and tidal mixing lead to very different patterns in the temperature and salinity change fields, respectively (see Figs. 6E versus Fig. 6B and C), respectively; despite similar AMOC strength changes (Fig. 4). This indicates that reconstructions of deep ocean properties may be used to infer the mechanism of AMOC changes.

When both LGM ICE-5G tide forcing and PMIP3 wind forcing are applied (lgm_i5gT_lgmW) the strength of the AMOC increases by a further 2.7 Sv and by 1.1 Sv for LGM ICE-6G tide forcing in lgm_i6gT_lgmW (Table 2). When LGM tide forcing is added to lgm_pdT_lgmW instead of lgm_pdT_pdW the increases in the AMOC are approximately halved for both LGM tide scenarios. This suggests that a stronger Atlantic overturning is less sensitive to changes in external forcing than a weak AMOC. This emphasizes the non-linearity of the responses of the circulation to different forcing. In lgm_pdT_lgmW Atl AABW has a strength of -3.1 Sv (-16%), in lgm_i5gT_lgmW it weakens to -2.2 Sv and is slightly stronger in lgm_i6gT_lgmW (-3.2 Sv) (Table 2).

With LGM wind forcing CPDW export into the Pacific is enhanced by ~1 Sv in comparison to the simulations using PD winds due to enhanced export of NADW into the Southern Ocean. The strong temperature decreases in the upper 3000 m north of 40°S in the Atlantic induced by the LGM wind forcing are somewhat reduced and warming and salinification of bottom waters result from LGM tidal forcing (Fig. 6).

Sea ice is more extensive in all LGM simulations in comparison to the PIC both in the southern and northern hemisphere (Suppl. Fig. S7) which is consistent with studies such as *Vettoretti and Peltier* [2013]. The simulations with PD winds show an increase in sea ice concentrations when LGM tides are applied whereas for runs with LGM wind forcing sea ice concentrations show no sensitivity to tidal forcing changes.

Discussion

Here, we have investigated the impact of LGM tidal dissipation changes on the overturning circulation using two different sea-level reconstructions. Our tide model simulations show that LGM dissipation is highly sensitive to the extent of the ice sheets adjoining the Atlantic, whereas it is much less sensitive to different parameterizations of internal wave drag and stratification. Whilst ICE-5G and ICE-6G show considerable differences both in the global mean sea-level decrease and the spatial patterns it appears that the ice sheet extent in the Weddell Sea and the extent of the Laurentide Ice Sheet have the greatest impact on both North and South Atlantic dissipation values. This is consistent with results by *Green* [2010], *Arbic et al.* [2004] and *Arbic et al.* [2009] showing that blocking shelf-seas in the present-day ocean without altering sea-level leads to large dissipation and amplitude increases due to the near resonant state of the Atlantic. Currently, considerable uncertainty exists in reconstructions of ice extent in the Weddell Sea during the LGM with recent work [*Hillenbrand et al.*, 2014] suggesting two different but equally likely scenarios; one where ice is grounded at the shelf break and one where grounded ice occupies only part of the continental shelf. *Le Brocq et al.* [2011] and *Whitehouse et al.* [2017] suggest that it was unlikely that the Weddell Sea was covered by ice grounded to the continental

shelf break during the Last Glacial for lengthy time periods. This would make the high

dissipation ICE-5G scenario more likely. However, it does not rule out periods during

which ice advanced to the shelf break and consequently lowered Atlantic dissipation, nor

periods of less extensive ice and increased tidal dissipation. Furthermore, as our results

emphasize that the amount by which tidal mixing increases during the LGM, especially in

the Atlantic, is dependent on ice extent both in the Weddell Sea and of the Laurentide Ice

Sheet. This suggests that repeated changes in ice extent in the northern and/or southern

hemisphere during the glacial period such as during Heinrich events, may have affected

dissipation and hence tidal mixing, leading to alterations in the strength and depth of the

MOC and hence further climate feedbacks.

Montenegro et al. [2007] conclude that changes in tidal dissipation have little effect on

the LGM overturning circulation. In contrast, *Schmittner et al.* [2015] and this study,

using arguably more realistic LGM tidal forcing with substantial Atlantic dissipation

enhancements, find a strong AMOC sensitivity to LGM dissipation changes. We have

carried out sensitivity simulations using a setup similar to *Montenegro et al.* [2007] (see

Suppl. Text S1 for details and results) and find that the low resolution of the tide model

together with the older bathymetry used leads to a reduced response in the climate model,

albeit not as weak as the responses seen in *Montenegro et al.* [2007], which additionally

may be linked to the presence of a subgridscale tidal mixing parameterization in our

model. This highlights the necessity to simulate tides at a high enough resolution in order

to capture tidal changes in enough detail.

Our climate model simulations forced with high-resolution tidal dissipation fields high-light that the MOC in the model is sensitive to the exact tide forcing applied for the LGM. Using present-day tides results in a weak and shoaled AMOC, whereas applying ICE-5G and ICE-6G tide forcing leads to a strengthening of the overturning by several Sverdrups to just below present-day levels. Increasing tidal dissipation strongly increases Atlantic diapycnal diffusivities, especially at mid latitudes in the North and South Atlantic where the tidal dissipation increases are strongest, and therefore enhances both the downward mixing of NADW and the mixing of southern and northern sourced waters. This becomes evident from the Atlantic temperature and salinity cross-sections shown in Fig. 6. However, as we do not change the background diffusivity k_{bg} with increased tidal mixing, our estimates of k_v and AMOC strength are likely to be conservative as they do not included the effects of changes in remotely dissipated tidal energy fluxes. The mixing efficiency and the fraction of energy dissipating locally are kept constant in this model setup, which is likely a limitation (see e.g., *Mashayek et al.* [2017]). Future work will address these issues. Furthermore, including more realistic LGM tidal mixing increases temperatures in the vicinity of the Antarctic Ice Sheet in the upper water column in some regions, especially in the Amundsen Sea and along the George coast, with the strongest enhancements occurring for the combination of tide and wind forcing. The temperature increases along the margins of Antarctica between 200 and 500 m are small (on the order of 0.1-0.4°C; see Suppl. Fig. S6), however, on a similar magnitude as those shown by *Bakker et al.* [2017] to evoke considerable changes in Antarctic Ice Sheet discharge, and AABW and NADW formation. The subsurface temperature increases along the Antarctic Ice Sheet margins could alter

520 Antarctic ice extent through melting of its floating ice shelves [*Holland et al.*, 2008], which

521 could lead to changes in tidal mixing and thus the global MOC, which in turn could evoke

522 feedbacks on the temperature field and therefore ice sheet extent *Menviel et al.* [2010].

These temperature changes may also have played a role during the deglacial period when

sea level rose and ice sheet extent changed (see e.g. *Golledge et al.* [2012]).

525 Recent work suggests a shallower but stable LGM MOC [*Gebbie*, 2014], possibly with a

526 weakened NADW flow in comparison to present with an increased proportion of AABW

527 in the deep Atlantic [*Howe et al.*, 2016; *Lippold et al.*, 2012; *Lynch-Stieglitz*, 2017; *Muglia*

al., 2018]. In order to counteract the increased tidal mixing and the resulting strength-

529 ing of the circulation, a mechanism strengthening the influx of southern-sourced water

530 to the North Atlantic would be needed, such as changes in the Southern Hemisphere

531 moisture flux [*Sigman et al.*, 2007] or reduced melting of ice shelves [*Miller et al.*, 2012;

kins, 2013]. Such a mechanism, which is not included in our experiments, may also

explain reconstructions of increased bottom water salinities [*Adkins et al.*, 2002] as shown

534 by *Muglia et al.* [2018].

535 Increased Atlantic diffusivities have generally been discounted as an explanation of

different abyssal water properties. *Howe et al.* [2016], for example, conclude that, due to

the large amounts of energy required, mixing of glacial North Atlantic intermediate waters

538 (GNAIW) with southern-sourced waters to abyssal depths is unlikely. They propose two

539 water masses - Glacial NADW - with different properties to GNAIW - and GNAIW.

Ferrari et al. [2014] suggest reduced mixing of AABW and NADW due to a shoaling

541 of their boundary, but they do not consider increases in tidal mixing. However, our

simulations suggest that strongly enhanced Atlantic diffusivities could be a likely feature of the glacial ocean, given the tidal changes that would be expected from bathymetry reconstructions.

Including LGM wind anomalies leads to a deepening and strengthening of the AMOC by strengthening the subtropical and subpolar gyre circulation in the North Atlantic which increases northward salt flux and increases salinities around 60° N. This is consistent with the findings by *Muglia and Schmittner* [2015] and *Ullman et al.* [2014]. However, in LGM_i5gT_lgmW and LGM_i6gT_lgmW the increased tidal mixing leads to a decrease in strength of the subpolar gyre suggesting that tidal mixing can influence the strength of the Atlantic gyre circulation both positively and negatively. Whilst our simulations suggest that wind and tidal forcing interact (non-linearly) with the gyre systems and that there may be a link between AMOC strength and gyre circulation as previously suggested e.g. *Joyce and Zhang* [2010], further exploration of this issue is beyond the scope of this paper and will be subject to future research.

Future work will include biogeochemistry and isotopes in the simulations in order to investigate the impacted of altered tidal mixing on corresponding tracer distributions in the LGM ocean, which can be directly compared to reconstructions from sediments. This will allow for a quantitative evaluation of the different circulations. We will also address limitations in the climate model set up used here. The simplified atmosphere prevents some feedbacks between ocean and atmosphere, and our model setup currently uses present-day bathymetry. Repeating a selection of experiments with a fully-coupled global climate model allowing for feedbacks between the different components in the climate system in

a format comparable to e.g. the PMIP3 simulations would be a useful extension of this work.

5. Conclusions

Here, we have investigated the impact of tidal dissipation changes on the LGM MOC using numerical models. Our tide model simulations show that large enhancements in tidal dissipation (1.1 - 2.4 TW or 85 - 200%) occur mainly in the Atlantic and that the magnitude of those increases are sensitive to LGM ice sheet extent. Better knowledge of LGM ice sheet grounding line extent, particularly in the Weddell Sea, but also of the ice sheets in the Northern Hemisphere would improve future estimates of tidal dissipation in the South Atlantic and in the North Atlantic.

Implementing the LGM tidal dissipation changes into a climate model leads to large increase in diapycnal diffusivities and a substantially strengthened AMOC. Export of NADW to the Southern Ocean at 32°S, e.g., increases by 1.5-5.2 Sv or 14-62%. LGM tides increase mixing between northern- and southern-sourced waters in the Atlantic, which cools the upper ocean and warms the abyss, processes ignored in current theories [*Ferrari et al.*, 2014] and most climate model simulations of LGM MOC changes. This work has important implications for future paleoclimate (modeling) studies suggesting that tidal dissipation changes need to be taken into account when investigating glacial ocean circulation. Altered mixing of the deep ocean will also affect biogeochemical cycles (see e.g. discussion in *Mashayek et al.* [2017]) and should be considered in future studies of the glacial ocean's carbon cycle.

References

Adkins, J. F., K. McIntyre, and D. P. Schrag (2002), The salinity, temperature, and delta18O of the glacial deep ocean., *Science (New York, N.Y.)*, *298*(5599), 1769–73, doi:10.1126/science.1076252.

Adkins, J. F. (2013), The role of deep ocean circulation in setting glacial climates, *Paleoceanography*, *28*, 539–561, doi:10.1002/palo.20046.

Arbic, B. K., D. R. Macayeal, J. X. Mitrovica, and G. A. Milne (2004), Palaeoclimate: ocean tides and Heinrich events., *Nature*, *432*, 460.

Arbic, B. K., R. H. Karsten, and C. Garrett (2009), On tidal resonance in the global ocean and the back-effect of coastal tides upon open-ocean tides, *Atmosphere-Ocean*, *47*, 239–266, doi:10.3137/OC311.2009.

Argus, D. F., W. R. Peltier, R. Drummond, A. W. Moore, and D. F. Argus (2014), The Antarctica component of postglacial rebound model ICE-6G_C (VM5a) based on GPS positioning, exposure age dating of ice thicknesses, and relative sea level histories, *Geo-*

physical Journal International Geophys. J. Int, *198*, 537–563, doi:10.1093/gji/ggu140.

Bakker, P., P. U. Clark, N. R. Golledge, A. Schmittner, and M. E. Weber (2017), Centennial-scale Holocene climate variations amplified by Antarctic Ice Sheet discharge, *Nature*, *541*(7635), 72–76, doi:10.1038/nature20582.

Bell, T. H. (1975), Topographically generated internal wave in the open ocean, *Journal of Geophysical Research*, *80*, 320–327.

Bradtmiller, L. I., J. F. McManus, and L. F. Robinson (2014), 231Pa/230Th evidence for a weakened but persistent Atlantic meridional overturning circulation during Heinrich Stadial 1, *Nature Communications*, *5*, 5817, doi:10.1038/ncomms6817.

Clark, P. U., A. S. Dyke, J. D. Shakun, A. .E Carlson, J. Clark, B. Wohlfarth, J. X. Mitrovica, S. W. Hostetler, and A. M. McCabe (2009), The Last Glacial Maximum, *Science*, *325*, 710–714, doi:10.1126/science.1172873.

Curry, W. B., and D. W. Oppo (2005), Glacial water mass geometry and the distribution of $\delta 13$ C of $\Sigma CO\ 2$ in the western Atlantic Ocean, *Paleoceanography*, *20*(1), PA1017, doi:10.1029/2004PA001021.

Eby, M., K. Zickfeld, A. Montenegro, D. Archer, K. J. Meissner, A. J. Weaver, M. Eby, K. Zickfeld, A. Montenegro, D. Archer, K. J. Meissner, and A. J. Weaver (2009), Lifetime of Anthropogenic Climate Change: Millennial Time Scales of Potential CO 2 and Surface Temperature Perturbations, *Journal of Climate*, *22*(10), 2501–2511, doi:10.1175/2008JCLI2554.1.

Egbert, G. D., and S. Y. Erofeeva (2002), Efficient inverse Modeling of barotropic ocean tides, *Journal of Atmospheric and Oceanic Technology*, *19*, 183–204.

Egbert, G. D., and R. D. Ray (2001), Estimates of M2 tidal energy dissipation from TOPEX/Poseidon altimeter data, *Journal of Geophysical Research*, *106*(C10), 22,475–22,502.

Egbert, G. D., and R. D. Ray (2003), Semidiurnal and diurnal tidal dissipation from TOPEX/POSEIDON altimetry, *Geophysical Research Letters*, *3017*, 1907, doi: 10.1029/2003GL017,676.

Egbert, G. D., A. F. Bennet, and M. G. G. Foreman (1994), Topex/Poseidon tides estimated using a global inverse model, *Journal of Geophysical Research*, *99*, 24,821–24,852.

Egbert, G. D., B. G. Bills, and R. D. Ray (2004), Numerical modeling of the global semidiurnal tide in the present day and in the last glacial maximum, *Journal of Geophysical Research*, *109*, C03,003, doi: 10.1029/2003JC001,973.

Ferrari, R., M. F. Jansen, J. F. Adkins, A. Burke, A. L. Stewart, and A. F. Thompson (2014), Antarctic sea ice control on ocean circulation in present and glacial climates, *Proceedings of the National Academy of Sciences*, *111*(24), 8753—8758.

Gebbie, G. (2014), How much did Glacial North Atlantic Water shoal?, *Paleoceanography*, *29*(3), 190–209, doi:10.1002/2013PA002557.

Gherardi, J.-M., L. Labeyrie, S. Nave, R. Francois, J. F. McManus, and E. Cortijo (2009), Glacial-interglacial circulation changes inferred from 231 Pa/ 230 Th sedimentary record in the North Atlantic region, *Paleoceanography*, *24*(2), PA2204, doi: 10.1029/2008PA001696.

Golledge, N. R., C. J. Fogwill, A. N. Mackintosh, and K. M. Buckley (2012), Dynamics of the last glacial maximum Antarctic ice-sheet and its response to ocean forcing., *Proceedings of the National Academy of Sciences of the United States of America*, *109*(40), 16,052–6, doi:10.1073/pnas.1205385109.

Green, J. A., M. Huber, D. Waltham, J. Buzan, and M. Wells (2017), Explicitly modelled deep-time tidal dissipation and its implication for Lunar history, *Earth and Planetary Science Letters*, *461*, 46–53, doi:10.1016/j.epsl.2016.12.038.

Green, J. A. M. (2010), Ocean tides and resonance, *Ocean Dynamics*, *60*(5), 1243–1253, doi:10.1007/s10236-010-0331-1.

Green, J. A. M., and M. Huber (2013), Tidal dissipation in the early Eocene and implications for ocean mixing, *Geophysical Research Letters*, *40*(11), 2707–2713, doi:10.1002/grl.50510.

Green, J. A. M., and J. Nycander (2013), A Comparison of Tidal Conversion Parameterizations for Tidal Models, *Journal of Physical Oceanography*, *43*(1), 104–119, doi:10.1175/JPO-D-12-023.1.

Green, J. A. M., C. L. Green, G. R. Bigg, T. P. Rippeth, J. D. Scourse, and K. Uehara (2009), Tidal mixing and the Meridional Overturning Circulation of the Last Glacial Maximum., *Geophysical Research Letters*, *36*, L15,603, doi:10.1029/2009GL039,309.

Griffiths, S. D., and W. R. Peltier (2009), Modeling of polar ocean tides at the Last Glacial Maximum: amplification, sensitivity, and climatological implications, *Journal of Climate*, *22*, 2905–2924, doi:10.1175/2008JCLI2540.1.

Hillenbrand, C.-D., M. J. Bentley, T. D. Stolldorf, A. S. Hein, G. Kuhn, A. G. Graham,

C. J. Fogwill, Y. Kristoffersen, J. A. Smith, J. B. Anderson, R. D. Larter, M. Melles,

D. A. Hodgson, R. Mulvaney, and D. E. Sugden (2014), Reconstruction of changes in

the Weddell Sea sector of the Antarctic Ice Sheet since the Last Glacial Maximum,

Quaternary Science Reviews, *100*, 111–136, doi:10.1016/j.quascirev.2013.07.020.

Holland, D. M., R. H. Thomas, B. deYoung, M. H. Ribergaard, B. Lyberth (2008),

Acceleration of Jakobshavn Isbrae triggered by warm sub-surface ocean waters *Nature

Geoscience*, *1*, 659–664.

Howe, J. N. W., A. M. Piotrowski, T. L. Noble, S. Mulitza, C. M. Chiessi, and G. Bayon

(2016), North Atlantic Deep Water Production during the Last Glacial Maximum,

Nature Communications, *7*, 11,765, doi:10.1038/ncomms11765.

Jayne, S. R., and L. C. St.Laurent (2001), Parameterizing tidal dissipation over rough

topography, *Geophysical Research Letters*, *28*, 811–814.

Joyce, T. M., and R. Zhang (2010), On the Path of the Gulf Stream and the At-

lantic Meridional Overturning Circulation, *Journal of Climate*, *23*(11), 3146–3154,

doi:10.1175/2010JCLI3310.1.

Kageyama, M., S. Albani, P. Braconnot, S. P. Harrison, P. O. Hopcroft, R. F.

Ivanovic, F. Lambert, O. Marti, W. Richard Peltier, J. Y. Peterschmitt, D. M. Roche,

L. Tarasov, X. Zhang, E. C. Brady, A. M. Haywood, A. N. Legrande, D. J. Lunt,

N. M. Mahowald, U. Mikolajewicz, K. H. Nisancioglu, B. L. Otto-Bliesner, H. Renssen,

R. A. Tomas, Q. Zhang, A. Abe-Ouchi, P. J. Bartlein, J. Cao, Q. Li, G. Lohmann,

R. Ohgaito, X. Shi, E. Volodin, K. Yoshida, X. Zhang, and W. Zheng (2017), The

PMIP4 contribution to CMIP6 - Part 4: Scientific objectives and experimental design of the PMIP4-CMIP6 Last Glacial Maximum experiments and PMIP4 sensitivity experiments, *Geoscientific Model Development*, *10*(11), 4035–4055, doi:10.5194/gmd-10-4035-2017.

Keigwin, L. D. (2004), Radiocarbon and stable isotope constraints on Last Glacial Maximum and Younger Dryas ventilation in the western North Atlantic, *Paleoceanography*, *19*(4), PA4012, doi:10.1029/2004PA001029.

Kurahashi-Nakamura, T., A. Paul, and M. Losch (2017), Dynamical reconstruction of the global ocean state during the Last Glacial Maximum, *Paleoceanography*, *32*(4), 326–350, doi:10.1002/2016PA003001.

Le Brocq, A. M., M. J. Bentley, A. Hubbard, C. J. Fogwill, D. E. Sugden, and P. L. Whitehouse (2011), Reconstructing the Last Glacial Maximum ice sheet in the Weddell Sea embayment, Antarctica, using numerical modelling constrained by field evidence, *Quaternary Science Reviews*, doi:10.1016/j.quascirev.2011.05.009.

Lippold, J., Y. Luo, R. Francois, S. E. Allen, J. Gherardi, S. Pichat, B. Hickey, and H. Schulz (2012), Strength and geometry of the glacial Atlantic Meridional Overturning Circulation, *Nature Geoscience*, *5*(11), 813–816, doi:10.1038/ngeo1608.

Locarnini, R. A., A. V. Mishonov, J. I. Antonov, T. P. Boyer, H. E. Garcia, O. K. Baranova, M. M. Zweng, C. R. Paver, J. R. Reagan, D. R. Johnson, M. Hamilton, and D. Seidov (2013), *World Ocean Atlas 2013, Volume 1: Temperature*, 40 pp., NOAA Atlas NESDIS 73.

713 Lumpkin, R., and K. Speer (2007), Global Ocean Meridional Overturning, *Journal of*

714   *Physical Oceanography*, *37*(10), 2550–2562, doi:10.1175/JPO3130.1.

715 Lynch-Stieglitz, J. (2017), The Atlantic Meridional Overturning Circulation and

         Abrupt Climate Change, *Annual Review of Marine Science*, *9*(1), 83–104, doi:

         10.1146/annurev-marine-010816-060415.

718 Marchitto, T. M., and W. S. Broecker (2006), Deep water mass geometry in the glacial

719   Atlantic Ocean: A review of constraints from the paleonutrient proxy Cd/Ca, *Geo-*

720   *chemistry, Geophysics, Geosystems*, *7*(12), Q12,003, doi:10.1029/2006GC001323.

         Mashayek, A., H. Salehipour, D. Bouffard, C. P. Caulfield, R. Ferrari, M. Nikurashin,

722   V. R. Peltier, and W. D. Smyth (2017), Efficiency of turbulent mixing in

723   the abyssal ocean circulation, *Geophysical Research Letters*, *44*, 6296–6306, doi:

724   10.1002/2016GL072452.

         McCarthy, G., E. Frajka-Williams, W. E. Johns, M. O. Baringer, C. S. Meinen, H. L.

726   Bryden, D. Rayner, A. Duchez, C. Roberts, and S. A. Cunningham (2012), Observed

727   interannual variability of the Atlantic meridional overturning circulation at 26.5°N,

728   *Geophysical Research Letters*, *39*(19), L19609, doi:10.1029/2012GL052933.

         Menviel, L., A. Timmermann, O. E. Timm, and A. Mouchet (2010), Climate and bio-

         geochemical response to a rapid melting of the West Antarctic Ice Sheet during in-

731   terglacials and implications for future climate, *Paleoceanography*, *25*, PA4231, doi:

732   10.1029/2009PA001892.

         Miller, M. D., J. F. Adkins, D. Menemenlis, and M. P. Schodlok (2012), The role of ocean

734   cooling in setting glacial southern source bottom water salinity, *Paleoceanography*, *27*,

PA3207, doi:10.1029/2012PA002297.

Montenegro, A., M. Eby, A. J. Weaver, and S. R. Jayne (2007), Response of a climate model to tidal mixing parameterization under present day and last glacial maximum conditions, *Ocean Modelling*, *19*, 125–137.

Muglia, J., and A. Schmittner (2015), Glacial Atlantic overturning increased by wind stress in climate models, *Geophysical Research Letters*, *42*(22), 9862–9868, doi: 10.1002/2015GL064583.

Muglia, J., L. C. Skinner, and A. Schmittner (2018), Weak overturning circulation and high Southern Ocean nutrient utilization maximized glacial ocean carbon, *Earth and Planetary Science Letters*, *496*, 47–56, doi:10.1016/j.epsl.2018.05.038.

Müller, M. (2008), Synthesis of forced oscillations, Part I: Tidal dynamics and the influence of the loading and self-attraction effect, *Ocean Modelling*, *20*(3), 207–222, doi:10.1016/j.ocemod.2007.09.001.

Müller, M., H. Haak, J. H. Jungclaus, J. Sündermann, and M. Thomas (2010) Normal Modes of the World Ocean. Part II: Description of Modes in the Period Range 8 to 80 Hours, *35*(4), 304–313, doi:10.1016/j.ocemod.2010.09.001.

Müller, M., J. Cherniawsky, M. Foreman, and J.-S. von Storch (2012), Global map of M2 internal tide and its seasonal variability from high resolution ocean circulation and tide modelling, *Geophysical Research Letters*, *39*, L19607, doi:10.1029/2012GL053320.

Nycander, J. (2005), Generation of internal waves in the deep ocean by tides, *Journal of Geophysical Research*, *110*, C10,028, doi:10.1029/2004JC002,487.

Otto-Bliesner, B. L., C. D. Hewitt, T. M. Marchitto, E. Brady, A. Abe-Ouchi, M. Crucifix, S. Murakami, and S. L. Weber (2007), Last Glacial Maximum ocean thermohaline circulation: PMIP2 model intercomparisons and data constraints, *Geophysical Research Letters*, *34*(12), L12,706, doi:10.1029/2007GL029475.

Pelling, H. E., and J. A. M. Green (2013), Sea level rise and tidal power plants in the Gulf of Maine, *Journal of Geophysical Research: Oceans*, *118*(6), 2863–2873, doi: 10.1002/jgrc.20221.

Peltier, W. R. (2004), Global glacial isostacy and the surface if the ice-age earth: The ICE-5G (VM2) model and Grace, *Annual Review of Earth and Planetary Sciences*, *32*, 111–149.

Peltier, W. R. and R. G. Fairbanks (2006),Global glacial ice volume and Last Glacial Maximum duration from an extended Barbados sea level record, *Quaternary Science Reviews*, *25*(23–24), 3322–3337, doi:10.1016/j.quascirev.2006.04.010.

Peltier, W. R., D. F. Argus, and R. Drummond (2015), Space geodesy constrains ice age terminal deglaciation: The global ICE-6G_C (VM5a) model, doi: 10.1002/2014JB011176.

Platzman, G. W., G. A. Curtis, K. S. Hansen, and R. D. Slater (1981), George W. Platzman, Gary A. Curtis, Kirk S. Hansen, and Richard D. Slater, *Journal of Physical Oceanography*, *11*, 579–603.

Schaffer, J., R. Timmermann, J. E. Arndt, S. S. Kristensen, C. Mayer, M. Morlighem, and D. Steinhage (2016), A global, high-resolution data set of ice sheet topography, cavity geometry, and ocean bathymetry, *Earth System Science Data*, *8*(2), 543–557,

778   doi:10.5194/essd-8-543-2016.

779 Schmittner, A., and G. D. Egbert (2014), An improved parameterization of tidal mixing

780   for ocean models, *Geoscientific Model Development*, *7*(1), 211–224, doi:10.5194/gmd-

        7-211-2014.

     Schmittner, A., J. A. M. Green, and S.-B. Wilmes (2015), Glacial ocean overturning

783   intensified by tidal mixing in a global circulation model, *Geophysical Research Letters*,

784   *42*(10), 4014–4022, doi:10.1002/2015GL063561.

785 Sigman, D. M., A. M. De Boer, and G. H. Haug (2007), Antarctic Stratification, At-

        mospheric Water Vapor, and Heinrich Events: A Hypothesis for Late Pleistocene

787   Deglaciations, in *Ocean Circulation: Mechanisms and Impacts - Past and Future*

788   *Changes of Meridional Overturning*, pp. 335–349, doi:10.1029/173GM21.

789 Sigman, D. M., M. P. Hain, and G. H. Haug (2010), The polar ocean and glacial cycles in

        atmospheric CO2 concentration, *Nature*, *466*(7302), 47–55, doi:10.1038/nature09149.

791 Simmons, H. L., S. R. Jayne, L. C. S. Laurent, and A. J. Weaver (2004), Tidally driven

792   mixing in a numerical model of the ocean general circulation, *Ocean Modelling*, *6*,

        245–263, doi:10.1016/S1463-5003(03)00011-8.

     Skinner, L. C., S. Fallon, C. Waelbroeck, E. Michel, and S. Barker (2010), Ventilation

        of the Deep Southern Ocean and Deglacial CO2 Rise, *Science*, *328*(5982), 1147–1151,

796   doi:10.1126/science.1183627.

797 Smith, W. H., and D. T. Sandwell (1997), Global Sea Floor Topography from Satel-

        lite Altimetry and Ship Depth Soundings, *Science*, *277*(5334), 1956–1962, doi:

799   10.1126/science.277.5334.1956.

Talley, L. D., G. L. Pickard, W. J. Emery, and J. H. Swift (2011), *Descriptive Physical Oceanography*, doi:10.1016/B978-0-7506-4552-2.10002-2.

Uehara, K., J. D. Scourse, K. J. Horsburgh, K. Lambeck, and A. P. Purcell (2006), Tidal evolution of the northwest European shelf seas from the Last Glacial Maximum to the present, *Journal of Geophysical Research*, *111*, C09,025, doi:10.1029/2006JC003,531.

Ullman, D. J., A. N. LeGrande, A. E. Carlson, F. S. Anslow, and J. M. Licciardi (2014), Assessing the impact of Laurentide Ice Sheet topography on glacial climate, *Climate of the Past*, *10*(2), 487–507, doi:10.5194/cp-10-487-2014.

 Toretti, G., and W. R. Peltier (2013), Last Glacial Maximum ice sheet impacts on North Atlantic climate variability: The importance of the sea ice lid, *Geophysical Research Letters*, *40*, 6378–6383, doi:10.1002/2013GL058486.

Waterhouse, A. F., J. A. MacKinnon, J. D. Nash, M. H. Alford, E. Kunze, H. L. Simmons, K. L. Polzin, L. C. St. Laurent, O. M. Sun, R. Pinkel, L. D. Talley, C. B. Whalen, T. N. Huussen, G. S. Carter, I. Fer, S. Waterman, A. C. Naveira Garabato, T. B. Sanford, C. M. Lee, A. F. Waterhouse, J. A. MacKinnon, J. D. Nash, M. H. Alford, E. Kunze, H. L. Simmons, K. L. Polzin, L. C. S. Laurent, O. M. Sun, R. Pinkel, L. D. Talley, C. B. Whalen, T. N. Huussen, G. S. Carter, I. Fer, S. Waterman, A. C. N. Garabato, T. B. Sanford, and C. M. Lee (2014), Global Patterns of Diapycnal Mixing from Measurements of the Turbulent Dissipation Rate, *Journal of Physical Oceanography*, *44*(7), 1854–1872, doi:10.1175/JPO-D-13-0104.1.

Weaver, A. J., M. Eby, E. C. Wiebe, C. M. Bitz, P. B. Duffy, T. L. Ewen, A. F. Fanning, M. M. Holland, A. MacFadyen, H. D. Matthews, K. J. Meissner, O. Saenko,

A. Schmittner, H. Wang, and M. Yoshimori (2001), The UVic earth system climate model: Model description, climatology, and applications to past, present and future climates, *Atmosphere-Ocean, 39*(4), 361–428, doi:10.1080/07055900.2001.9649686.

Weber, S. L., S. S. Drijfhout, A. Abe-Ouchi, M. Crucifix, M. Eby, A. Ganopolski, S. Murakami, B. Otto-Bliesner, and W. R. Peltier (2007), The modern and glacial overturning circulation in the Atlantic ocean in PMIP coupled model simulations, *Climate of the Past, 3*(1), 51–64.

Weber, T., and M. Thomas (2017), Influence of ocean tides on the general ocean circulation in the early Eocene, *Paleoceanography, 32*, 553–570, doi:10.1002/2016PA002997.

Whitehouse, P. L., M. J. Bentley, A. Vieli, S. S. R. Jamieson, A. S. Hein, and D. E. Sugden (2017), Controls on Last Glacial Maximum ice extent in the Weddell Sea embayment, Antarctica, *Journal of Geophysical Research: Earth Surface, 122*(1), 371–397, doi:10.1002/2016JF004121.

Wilmes, S.-B., and J. A. M. Green (2014), The evolution of tides and tidal dissipation over the past 21,000 years, *Journal of Geophysical Research: Oceans, 119*(7), 4083–4100, doi:10.1002/2013JC009605.

Wilmes, S.-B., J. A. M. Green, N. Gomez, T. P. Rippeth, and H. Lau (2017), Global tidal impacts of large-scale ice-sheet collapses, *Journal of Geophysical Research: Oceans, in press*, doi:10.1002/2017JC013109RR.

Wunsch, C. (2003), Determining paleoceanographic circulations, with emphasis on the Last Glacial Maximum, *Quaternary Science Reviews, 22*, 2371–2385.

Wunsch, C. (2016), Pore fluids and the LGM ocean salinity reconsidered, *Quaternary Science Reviews*, *135*, 154–170, doi:10.1016/j.quascirev.2016.01.015.

Wunsch, C., and R. Ferrari (2004), Vertical mixing, energy, and the general circulation of the oceans, *Annual Review of Fluid Mechanics*, *36*, 281–314, doi:10.1146/annurev.fluid.36.050,802.

Zaron, E. D., and G. D. Egbert (2006), Estimating open-ocean barotropic tidal dissipation: The Hawaiian Ridge, *Journal of Physical Oceanography*, *36*, 1019–1035.

Zweng, M., J. R. Reagan, J. I. Antonov, R. A. Locarni, A. V. Mishonov, T. P. Boyer, I. E. Garcia, O. K. Baranova, D. R. Johnson, D. Seidov, and M. M. Biddle (2013), *World Ocean Atlas 2013, Volume 2: Salinity*, 39 pp., NOAA Atlas NESDIS 74.
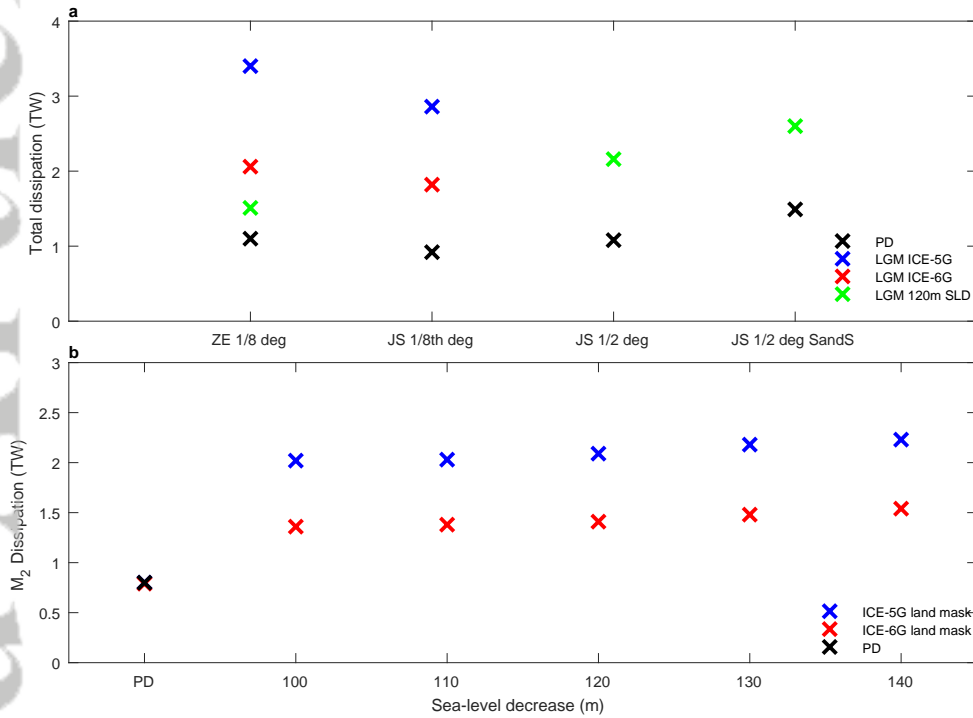
Figure 1. Globally integrated dissipation rates in waters greater than 500 m depth. (a) Total dissipation rates (sum of M_2, S_2, K_1 and O_1) for the present-day (PD; black crosses), LGM with ICE-5G bathymetry (blue crosses), LGM with ICE-6G bathymetry (red crosses), and a uniform 120 m SLD (gray crosses). For details on the simulations denoted JS 1/2 and JS 1/2 SandS please refer to Supplementary Text S1. (b) M_2 dissipation rates for simulations with ZE ITdrag and uniform SLD with either the LGM ICE-5G (blue crosses) or the LGM ICE-6G (red crosses) land mask.

Table 1. Set up of present-day tide model simulation set up and evaluation. Globally integrated dissipation values are given for the energy-balance method (EB) and for the direct method (DIR). 'Deep' refers to water depths greater than 500 m. For details on the simulations denoted PD_JS_1.2 and PD_JS_1.2_SS please refer to Supplementary Text S1.

Simulation	Time slice	Bathymetry	ITdrag	Resolution	Tuning factor	EB tot. dissip. (TW)	EB deep dissip. (TW)	DIR tot. dissip. (TW)	DIR deep dissip. (TW)	deep RMSE (cm)	total RMSE (cm)
TPXO8	PD	TPXO8		1/8°		3.14	1.15				
PD_ZE_1.8	PD	RTOPO2	ZE	1/8°	75	3.30	1.34	3.73	1.10	3.8	6.3
PD_JS_1.8	PD	RTOPO2	JS	1/8°	1667	3.19	1.19	2.91	0.92	4.5	8.8
PD_JS_1.2	PD	RTOPO2	JS	1/2°	10000	3.18	1.19	3.45	1.08	5.9	13.3
PD_JS_1.2_SS	PD	S&S	JS	1/2°	10000	3.31	1.22	2.78	1.41	6.0	10.4

Table 2. Ocean circulation indexes given in units of Sverdrups. The observational data comes from *Schmittner and Egbert* [2014] (see their Table 3) and is a compilation of data from *Lumpkin and Speer* [2007] and *McCarthy et al.* [2012]. "glob. deep" denotes the maximum meridional overturning stream function below 400 m depth, "AMOC 25°N" and "AMOC 32°S" give the maximum Atlantic meridional stream function below 300 m at 25°N and at 32°S, respectively. "ABBW Atl." gives the minimum meridional stream function below 1.5km at 35°S. "CPDW Ind." and "CPDW Pac." give the circumpolar deep water export into the Indian and Pacific Ocean, respectively, at 32°S. Positive (negative) values indicate a clockwise (counter-clockwise) overturning. RMSE represents the root-mean square of the differences between the observations and the PIC.

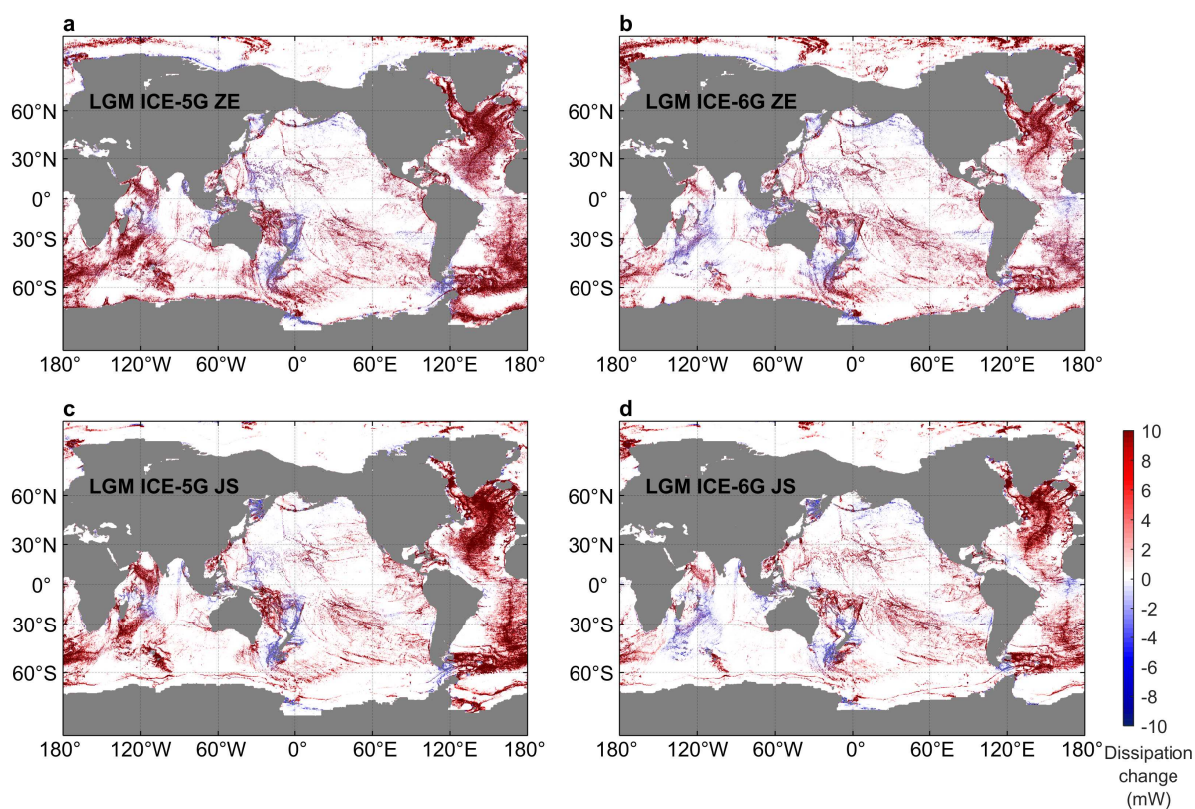| Simulation	glob. deep	AMOC 25°N	AMOC 32°S	AABW Atl.	CPDW Ind.	CPWD Pac.	RMSE (Sv)
observations	20.9±6.7	17.5±2.0	12.0±3.1	-5.6±3.0	-9.2±2.7	-11.0±5.1	
PIC	18.0	16.0	14.1	-4.0	-7.2	-9.5	2.0
LGM-pdT-pdW	13.0	10.2	8.3	-3.7	-5.4	-10.1	
LGM.i5gT-pdW	16.0	14.0	13.5	-3.2	-7.1	-11.2	
LGM.i6gT-pdW	14.3	13.0	10.8	-3.6	-5.4	-11.7	
LGM-pdT-lgmW	17.2	13.1	10.7	-3.1	-5.2	-10.7	
LGM.i5gT-lgmW	18.4	15.8	13.7	-2.2	-7.0	-12.2	
LGM.i6gT-lgmW	18.0	14.2	12.2	-3.2	-5.2	-12.9	

Figure 2. Change in dissipation rates (all constituents; sum of M_2, S_2, K_1 and O_1) with respect to present day for (a) LGM ICE-5G ZE ITdrag, (b) LGM ICE-6G ZE ITdrag, (c) LGM ICE-5G JS ITdrag and (d) LGM ICE-6G JS ITdrag.
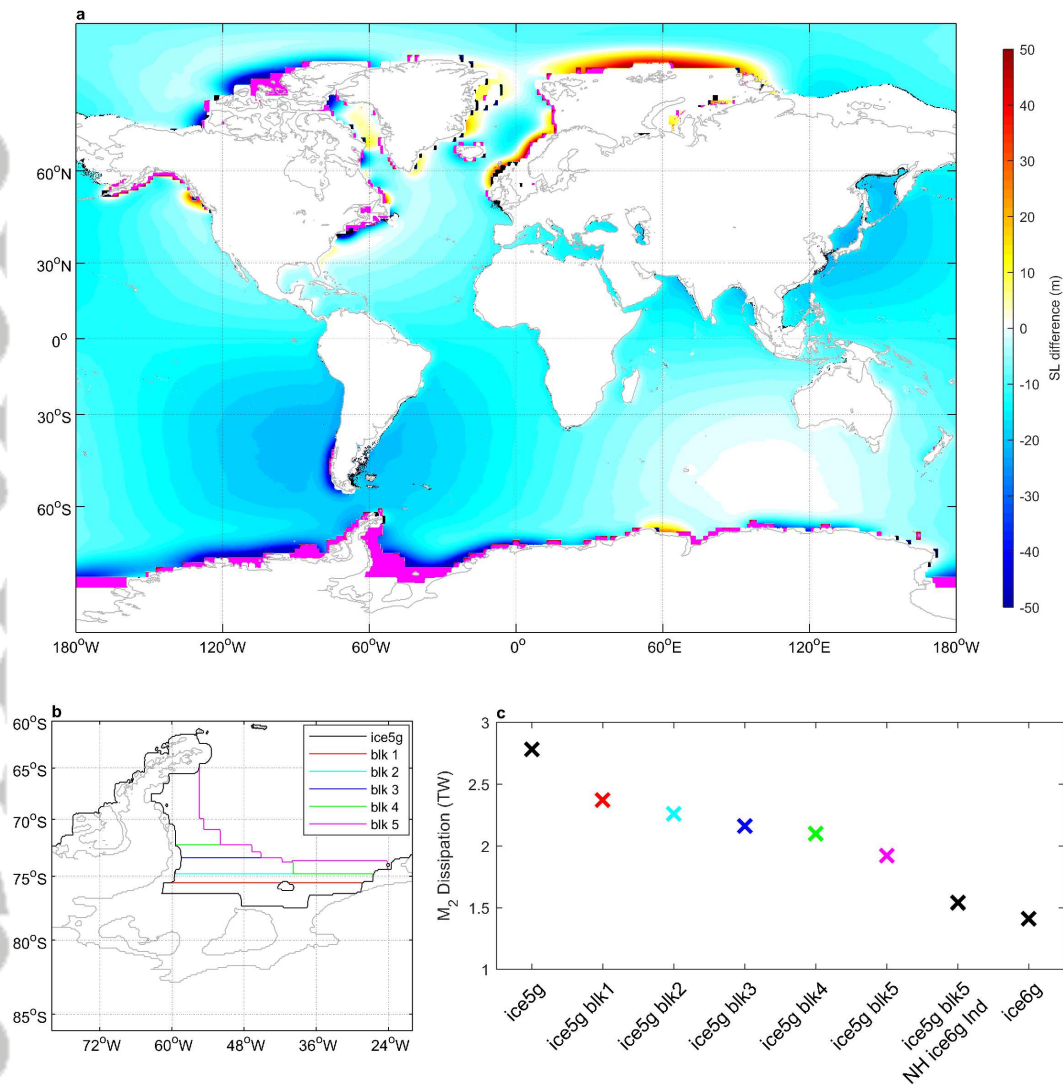
Figure 3. (a) Difference in sea-level between LGM ICE-5G and LGM ICE-6G. Pink shaded areas indicate locations where grounded ice exists in ICE-6G but not in ICE-5G, black shading shows areas where ice was grounded in ICE-5G but not in ICE-6G. Grey contours show the PD coastline. (b) Ice extent in the Weddell Sea for the ICE-5G blk 1 to blk 5 sensitivity simulations. The ICE-5G ice extent is contoured in black. Grey contours show the PD coastline. (c) M_2 dissipation rates for simulations where the Weddell Sea is incrementally blocked from the LGM ICE-5G case (blk 1 - blk5), and the ICE-6G land mask is applied in the northern hemisphere (ice5g blk5 + NH ice6g lnd).
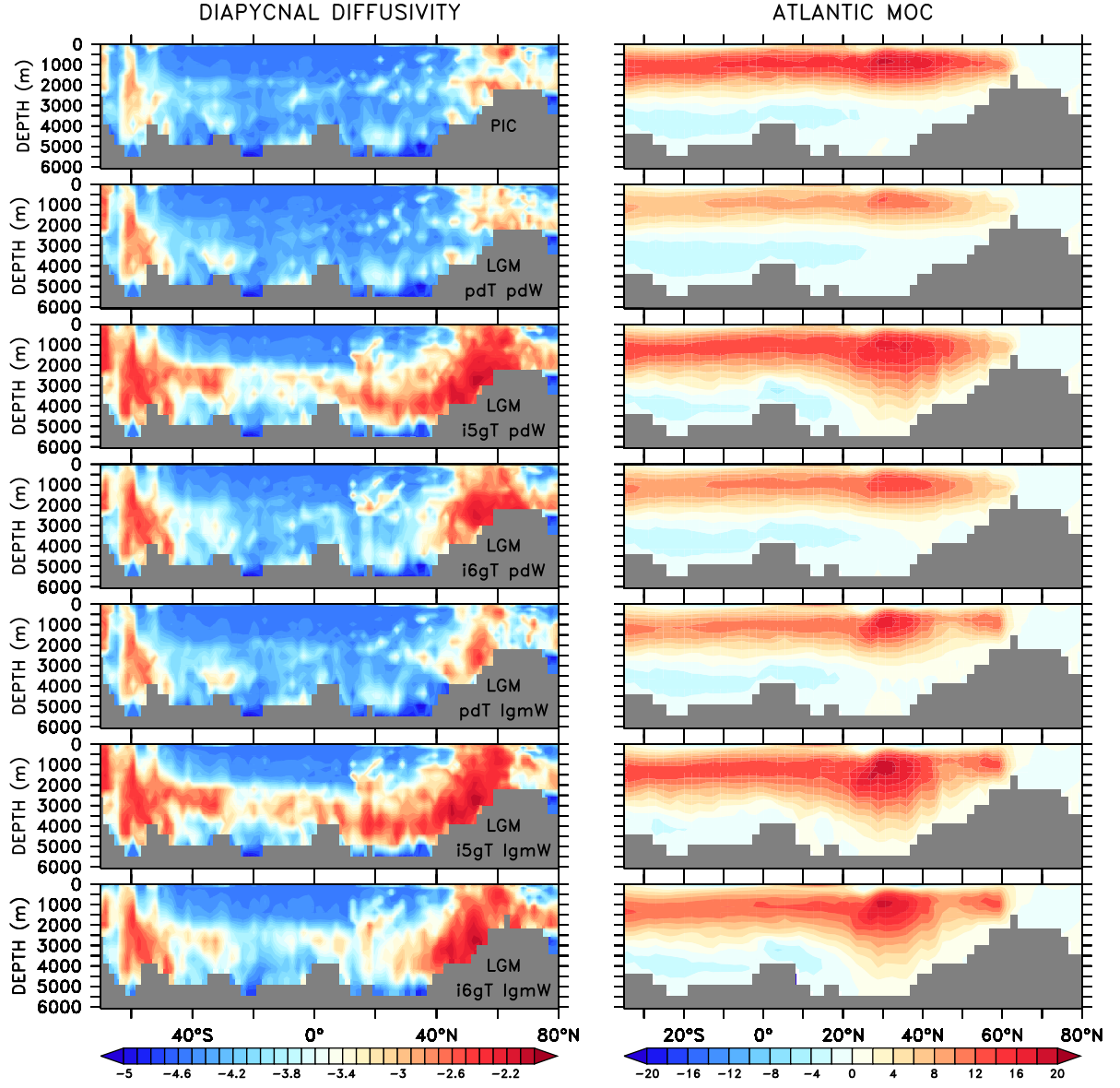
Figure 4.   (left) log$_{10}$ of zonally averaged diapycnal diffusivities (m^{2}s^{-1}) in the Atlantic and (right) AMOC strength (Sv) for (a) PIC, (b) LGM_pdT_pdW, (c) LGM_i5gT_pdW, (d) LGM_i6gT_pdW, (e) LGM_pdT_lgmW, (f) LGM_i5gT_lgmW and (g) LGM_i6gT_lgmW.
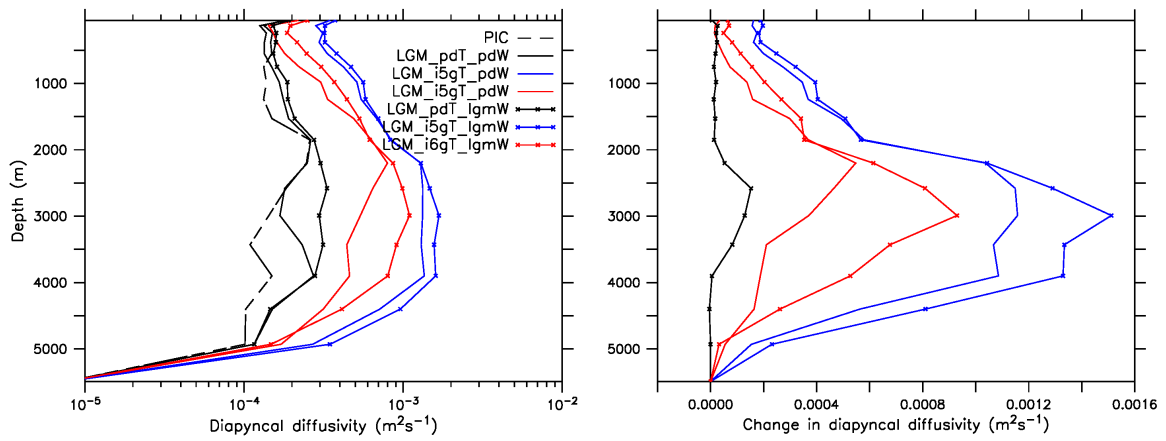
Figure 5. (a) Horizontally averaged Atlantic diapycnal diffusivities and (b) change in Atlantic diffusivities with respect to lgm_pdT_pdW.
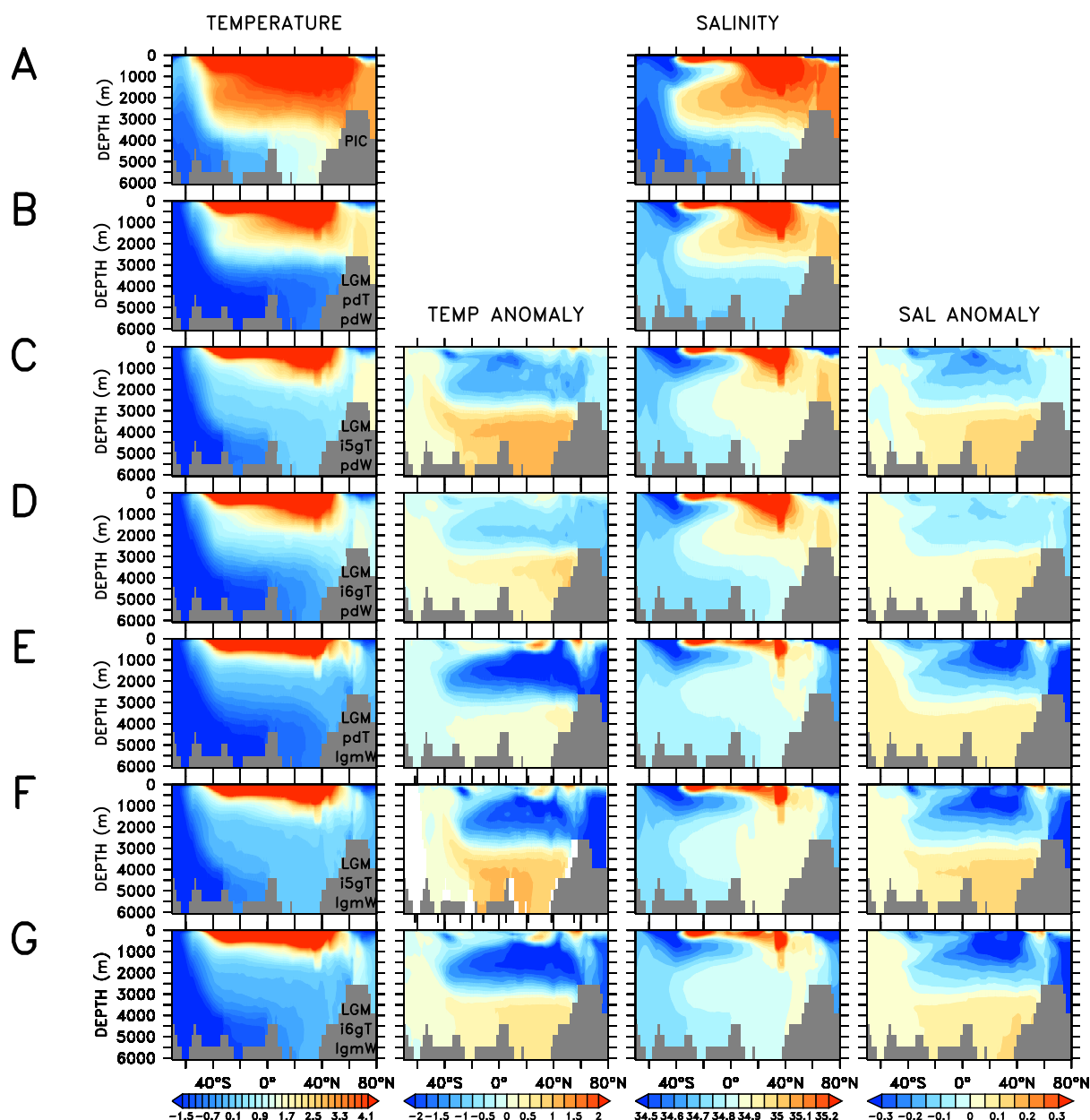
Figure 6. (1st column) Atlantic temperature (°C), (2nd column) Atlantic temperature anomalies with respect to LGM_pdT_pdW (°C), (3rd column) Atlantic salinities (psu) and (4th column) Atlantic salinity anomalies with respect to LGM_pdT_pdW (psu) for (a) PIC, (b) LGM_pdT_pdW, (c) LGM_i5gT_pdW, (d) LGM_i6gT_pdW, (e) LGM_pdT_lgmW, (f) LGM_i5gT_lgmW and (g) LGM_i6gT_lgmW.
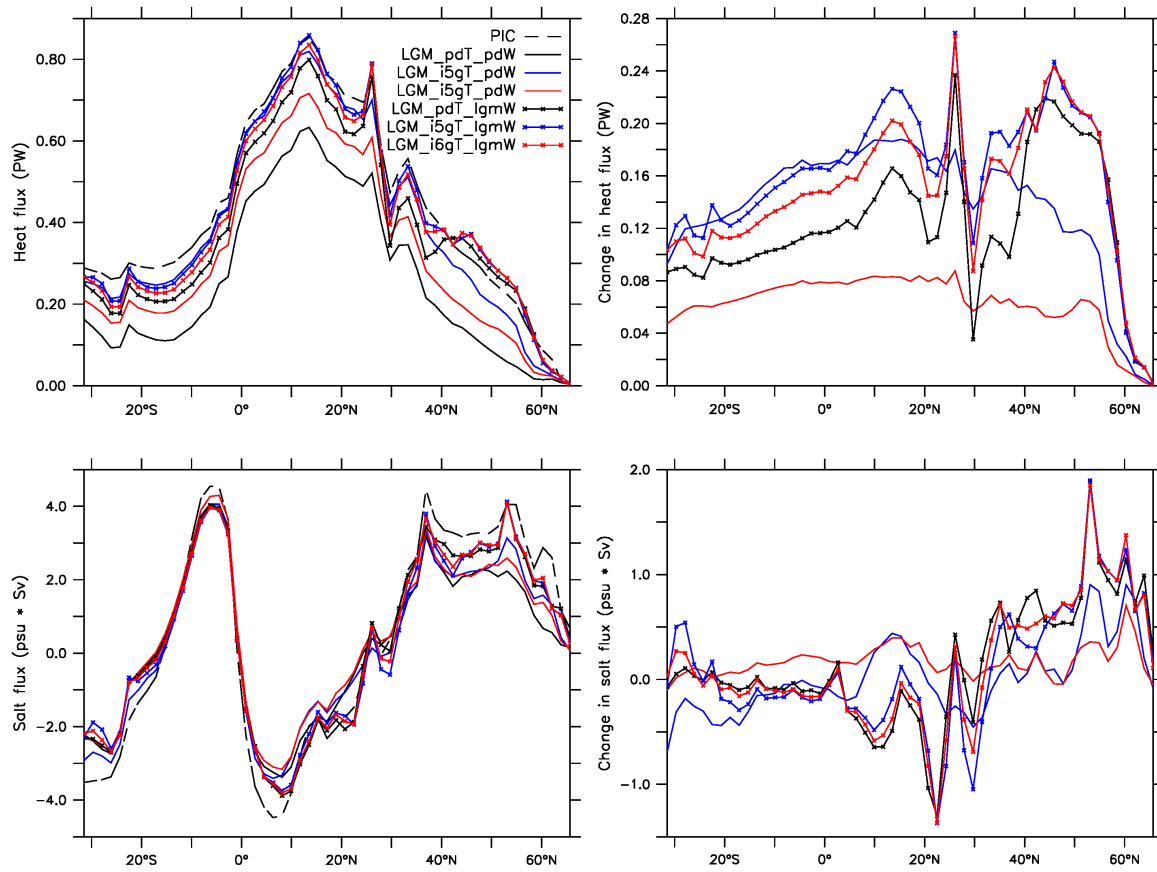
Figure 7. (a) Horizontally integrated Atlantic meridional heatflux and (b) change in Atlantic heat flux with respect to lgm_pdT_pdW. (c) Horizontally integrated Atlantic salt flux and (d) change in Atlantic salt flux with respect to lgm_pdT_pdW.